Forzieri, G.; Miralles, D.G.; Ciais, P.; Alkama, R.; Ryu, Y.; Duveiller, G.; Zhang, K.; Robertson, E.; Kautz, M.; Martens, B.; Jiang, C.; Arneth, A.; Georgievski, G.; Li, W.; Ceccherini, G.; Anthoni, P.; Lawrence, P.; Wiltshire, A.; Pongratz, J.; Piao, S.; Sitch, S.; Goll, D.S.; Arora, V.K.; Lienert, S.; Lombardozzi, D.; Kato, E.; Nabel, J.E.M.S.; Tian, H.; Friedlingstein, P.; Cescatti, A.:

Increased control of vegetation on global terrestrial energy fluxes.

In: Nature Climate Change. Vol. 10 (2020) 4, 356 - 362.
First published online by Nature Publishing Group: 16.03.2020

https://dx.doi.org/10.1038/s41558-020-0717-0

Increased control of vegetation on global terrestrial energy fluxes

Giovanni Forzieri[1,*], Diego G. Miralles[2], Philippe Ciais[3], Ramdane Alkama[1], Youngryel Ryu[4], Gregory Duveiller[1], Ke Zhang[5], Eddy Robertson[6], Markus Kautz[7], Brecht Martens[2], Chongya Jiang[4], Almut Arneth[8], Goran Georgievski[9,10], Wei Li[3], Guido Ceccherini[1], Peter Anthoni[8], Peter Lawrence[11], Andy Wiltshire[6], Julia Pongratz[12], Shilong Piao[13], Stephen Sitch[14], Daniel S. Goll[15], Vivek K. Arora[16], Sebastian Lienert[17], Danica Lombardozzi[11], Etsushi Kato[18], Julia E.M.S. Nabel[19], Hanqin Tian[20], Pierre Friedlingstein[21], Alessandro Cescatti[1]

[1] European Commission, Joint Research Centre, Ispra, Italy
[2] Laboratory of Hydrology and Water Management, Department of Environment, Ghent University, Belgium
[3] LSCE IPSL, Gif-sur-Yvette, France
[4] Department of Landscape Architecture and Rural Systems Engineering, Seoul National University, Seoul, Korea
[5] College of Hydrology and Water Resources, Hohai University, Nanjing, China
[6] Met Office, Exeter, United Kingdom
[7] Forest Research Institute Baden-Württemberg, Freiburg, Germany
[8] KIT, Garmisch-Partenkirchen, Germany
[9] Helmholtz-Zentrum Geesthacht, Institute of Coastal Research, Germany
[10] Alfred Wegener Institute, Helmholtz Centre for Polar and Marine Research, Germany
[11] NCAR, Boulder, Colorado, USA
[12] Ludwig-Maximilians-Universität München, Munich, Germany
[13] Department of Ecology, Peking University, China
[14] College of Life and Environmental Sciences, University of Exeter, Exeter, United Kingdom
[15] Department of Geography, University of Augsburg, Augsburg, Germany
[16] Canadian Centre for Climate Modelling and Analysis, Environment Canada, University of Victoria, Canada
[17] Climate and Environmental Physics, Physics Institute and Oeschger Centre for Climate Change Research, University of Bern, Switzerland
[18] Institute of Applied Energy (IAE), Tokyo, Japan
[19] MPI, Hamburg, Germany
[20] Solon & Martha Dixon Professor, Director of International Center for Climate and Global Change Research, School of Forestry and Wildlife Sciences, Auburn University, Alabama, USA
[21] College of Engineering, Mathematics and Physical Sciences, University of Exeter, Exeter, United Kingdom

*Correspondence to: Giovanni Forzieri (giovanni.forzieri@ec.europa.eu)

Vegetation structure changes are expected to influence heat and moisture redistribution, however how variations in leaf area index (*LAI*) affect this global energy partitioning is not yet quantified. Here, we estimate that a unit change of *LAI* leads to 3.66±0.45 and -3.26±0.41 Wm^{-2} in latent (*LE*) and sensible (*H*) fluxes, respectively, over 1982-2016. Analysis of an ensemble of data-driven products and land surface models (LSMs) shows these sensitivities increase by about 20% over the observational period, prominently in water supply-limited regions, likely because of an increased transpiration/evaporation ratio. Global greening has caused a decline in Bowen ratio ($B=H/LE$) of -0.010±0.002 per decade attributable to the increased evaporative surface. Such direct *LAI* effect on energy fluxes is largely modulated by plant functional types and background climate conditions. LSMs misrepresent this vegetation control possibly due to underestimation of the biophysical response to water availability changes and poor representation of *LAI* dynamics.

The surface energy partitioning, resulting from the conversion of available energy into latent (*LE*) and sensible (*H*) heat, exerts a strong control on the state of the atmospheric boundary layer, the lowest layer of the troposphere that is in contact with the surface of the Earth. It propagates changes in land surface properties to the atmosphere[1,2] by regulating land-atmosphere feedbacks and influencing the global cycles of water and energy[3]. While most research has been devoted to exploring the impact of soil moisture on surface energy partitioning[4,5], vegetation density can also play an important role in the modulation of the surface energy budget[6–8]. In fact, changes in vegetation structure and physiology associated with the ongoing global and persistent increase in leaf area index (*LAI*)[9] are expected to influence canopy conductance, aerodynamic properties and the albedo of ecosystems, ultimately affecting water and energy fluxes between land and atmosphere[10,11]. Consequent variations in climate modulate the interplay between *LAI*-related biophysical processes and the surface energy partitioning[12,13]. Rising atmospheric CO_2 concentration further affects the vegetation control on surface energy partitioning by reducing stomatal conductance[14] and therefore transpiration per unit of leaf area, ultimately leading to an increasing ratio of carbon gain to water loss (water-use efficiency, WUE)[15]. Although the influence of global greening feedbacks on surface temperature has been recognized and assessed[12,16], its more direct impacts on the surface energy partitioning at planetary level have not been explicitly explored yet.

Disentangling the role of *LAI* from the contribution of other direct drivers on the surface energy partitioning is challenging due to the variety of land-atmosphere interactions occurring over multiple spatial and temporal scales[17]. For this scope, the availability of observations from field experiments[18] and flux tower data[19] is limited in terms of number of stations and geographic coverage, allowing only the partial characterization of the spatio-temporal variability of the phenomena. On the modelling side, Land Surface Models (LSMs) – the land component of Earth System Models used to predict future climate trajectories – include *LAI* as a key prognostic variable and its interactions with surface biophysics, hydrology and biogeochemistry are represented through equations of varying complexity[20]. However, LSMs show important limitations in reproducing the interplay between vegetation and climate due to an incomplete understanding and model representation of biophysical processes[21,22]. These drawbacks inevitably hamper understanding of land-atmosphere interactions based on *in situ* observations and model predictions. Conversely, the increasing availability and accessibility of satellite remote sensing products that address the physical state of the land surface may overcome these limitations and offer robust global datasets for model evaluation and process understanding.

Here, we investigate the impacts of greening on *LE*, *H* and Bowen ratio (defined as $B=H/LE$) for 1982–2016 at the global scale, using four observation-driven products of evapotranspiration (*ET*) and climate drivers in combination with three long-term satellite *LAI* data sets. We refer to the growing season averaged *LAI* as a diagnostic variable of vegetation density. The sensitivity of *LE*, *H* and *B* to *LAI* changes is quantified as partial derivatives from multiple linear regressions ($\partial Z/\partial LAI$, where *Z* is any of the energy terms). The potentially confounding direct effect (not through *LAI*) of climate drivers like precipitation and temperature on *LE*, *H* and *B* has been factored out by considering these variables among the predictors of the linear model (Methods). Furthermore, interannual variations of both response variable and predictors have been used in the regression in order to rule out possible long-term dependencies between covariates. Long-term effects in surface energy terms attributable strictly to the greening (δZ^{LAI}) are then quantified by combining sensitivity estimates with long-term trends in *LAI*. Sensitivity ($\partial Z/\partial LAI$) and effects (δZ^{LAI}) are derived for each combination of *LAI* and energy flux datasets resulting in a 12-member ensemble of observation-based estimates. In order to account for differences across datasets[23], the ensemble average is calculated and the corresponding standard error is retrieved (Methods). Finally, we compared the metrics derived from satellite-based observations with those computed on factorial simulations of ten state-of-the-art LSMs, in order to assess the ability of models to represent the interplay between vegetation changes and surface energy partitioning (Methods).

Increased sensitivity of surface energy partitioning on *LAI*

Estimates of sensitivity of the energy partitioning terms to *LAI* (Eq. (1), Methods) quantified for the 1982–2016 period show a clear dependence on the background climate (Fig. 1a,d,g). Confirming previous model-based studies[6], the increase in *LAI* enhances *LE* globally (3.66±0.45 Wm^{-2} per unit of leaf area, Supplementary Table 1) and particularly in warm-dry regions, as a consequence of the increase in evaporative surface (Fig. 1a). In these regions, despite potential soil moisture limitation on *LE* due to low rainfall, at inter-annual timescale an increase in *LAI* is associated with an increase in *LE* through complex adjustments of *LAI* sustaining *LE*, such as root development, access to groundwater[24] and phenological seasonal shifts[25]. Given that *LE* and *H* represent competitive pathways for energy release from the land surface, *H* shows opposite patterns of sensitivity to *LAI* than *LE*, with an average negative sensitivity of -3.26±0.41 Wm^{-2} per unit of leaf area (Fig. 1d, Supplementary Table 1). Ultimately, changes in *B* are inversely related to *LAI* (-0.14±0.02 per unit of leaf area, Fig. 1g and Supplementary Table 1), since the increase in leaf area favors the dissipation of available energy by evaporating water, leading to surface cooling and a subsequent *H* reduction[12,16]. These findings emphasize the importance of interannual vegetation controls on climate, particularly during extreme events such as meteorological droughts and heatwaves, when a higher *LAI* can effectively dampen the increases in land surface temperature by evaporative cooling, yet at the expense of further drying out the soils[26].

Exploring the temporal variation of the sensitivities with moving windows of different amplitude (for brevity a 13-year window is shown here), we found substantial changes over the observational period, particularly from 2000 onwards (Fig. 1b,e,h). Globally we quantified a significant (p-value≤0.05) relative increase of 20-24% (Δ_{rel}) in the value of the sensitivity of energy fluxes to *LAI* over 2000–2016 versus 1982–1999 (gray circles in Fig. 1c,f,i), suggesting an increasing control of energy fluxes from terrestrial vegetation. Despite the relevant spread observed across single *LAI* products, global trends are largely consistent (Extended Data Fig. 1) and show a dependence of the variation in sensitivity to the changes in interannual *LAI* variability (Supplementary Fig. 1). Albeit we cannot exclude a possible contamination of the variability in *LAI* from the temporal variations in satellite platforms and sampling density, we stress that climate variations are very likely to play a major role on the emerging signal. This statement is supported by the analysis of the gradients in sensitivity across space (Extended Data Fig. 2, Methods). The dependence of the sensitivity on the aridity index over the two observation periods is statistically identical, despite the change in the observation system (from AVHRR to MODIS). These results further corroborates the relevance of climate change on the temporal variation of the sensitivity.

The possible mechanisms responsible for such emerging variations in sensitivity were investigated by disaggregating the signal for regions where evaporation is limited by atmospheric demand or by water supply (Methods). We found that the largest absolute variations occur in regions limited by the supply of moisture where the change of sensitivity is four-fold higher than in demand-limited regions (e.g., Δ_{abs} of sensitivity of *LE* ~1.8 and 0.4 Wm^{-2}, respectively, green and orange circles in Fig. 1c). The concomitant strong positive trends in temperature and moderately negative trends in precipitation lead to a progressive transition to warmer and drier conditions (Extended Data Fig. 3c-f), which is represented as a shift towards the upper-left corner in the panels Fig. 1a,d,g. In moisture supply-limited environments, such changes in climate background have likely increased the ratio between transpiration and evaporation leading to an enhanced biological control on evapotranspiration. This hypothesis is supported by the widespread increasing trend in the fraction of transpired water to the total evapotranspiration (Extended Data Fig. 3i,j) also documented in previous studies[27]. The recent climate-induced expansion of areas limited by water supply has presumably amplified this process (Extended Data Fig. 4a).

We found that, consistently with expectations, temporal changes in sensitivity are lower for the datasets that explicitly account for the direct CO_2 effects on stomatal conductance and transpiration (PLSH and BESS) than for the other products (GLEAM and MTE). However, a significant increase in sensitivity (Δ_{rel}>10%) emerges even for ET products that consider CO_2 effects (Fig. 1c,f,i and Extended Data Fig. 1), therefore suggesting that the increase in WUE[28] cannot fully offset the emerging climate signal of increasing control of plant leaves on terrestrial energy fluxes.

Greening plays a key role in surface energy partitioning

The effects of greening on surface energy partitioning are derived by multiplying the observed sensitivity by the long-term trend in growing season averaged *LAI* as quantified for the 1982–2016 period (Extended Data Fig. 3a,b and Extended Data Fig. 5a-c), i.e. by applying the methodology described in ref. [12] (Eq. (4), Methods). Results show that the variations in *LAI* occurring over the last three and a half decades led *per se* to a significant increase in *LE* over a large part of the globe (Fig. 2a,c), particularly in moisture supply-limited regions (0.41±0.09 $Wm^{-2}decade^{-1}$, Supplementary Table 1). Such a pronounced impact of greening results from the combination of moderately positive trends in *LAI* (Extended Data Fig. 3a,b) and the high sensitivity of the latent heat fluxes to *LAI* in those regions (Fig. 1a), consistently with previous findings[27,29]. In contrast, atmospheric demand-limited regions show a limited impact of *LAI* changes on *LE* trends (Fig. 2a,c), primarily due to the low sensitivity of evapotranspiration to *LAI* changes in these areas (Fig. 1a). As expected, trends in *H* associated with greening are opposite to those of *LE*, due to their reverse sensitivity (Fig. 2d,f). The combination of increasing *LE* and decreasing *H* trends attributable to the greening signal led to a widespread decline on *B* (-0.010±0.002 decade^{-1}, Supplementary Table 1) (Fig. 2g,i). Since these effects of *LAI* are larger in water-limited regions associated with high *B* values, the recent greening may have reduced the spatial variability of surface energy partitioning across the Earth, ultimately affecting the strength of the land-atmosphere coupling and the dynamics of the boundary layer.

The seasonality of the sensitivity show peak values at the onset of the growing season, particularly in Northern Hemisphere temperate regions (Fig. 2b,e,h). This suggests that during the growing season the partition of surface available energy is more closely controlled by variations in *LAI*, mainly due to the increase in the ratio of transpiration to evaporation. Climate driven changes in plant phenology may further amplify these mechanisms, particularly at the beginning of the growing season due to the expected increase in transpiration associated to the earlier onset of vegetation green-up[30]. Furthermore, we note that the *LAI*-related trend in energy partitioning shows a modest seasonal pattern also at high-latitudes with a change in sign that is more evident for *LE* (Fig. 2b,e). In this climate zone, the interplay between *LAI* and energy partitioning seems to be dominated by radiative terms during cold seasons (*LAI*-related reduction in albedo increasing *H* / decreasing *LE* during condition of snow cover), but still by changes in evaporative surface during the warm seasons (strong positive control of *LAI* on transpiration), consistently with previous studies[31].

The methodology used to quantify the effects of long-term trends of *LAI* on surface energy partitioning at annual level is then applied to each predictor of the regression to assess their relative contributions. A large variability across supply- and demand-limited zones emerges for the effects associated with *LAI*, air temperature (*T*), precipitation (*P*) and short-wave incoming radiation (SW_{IN}) (Fig. 3a-c), reflecting the spatial variations in long-term trends and sensitivity of each variable (Extended Data Fig. 3 and Extended Data Fig 5). While our assessment neglects possible interactions amongst drivers, it unequivocally shows that *LAI* plays a larger control than direct effects of *T*, *P* and radiation on the trends in energy fluxes (Fig. 3a-c). Notably, the low contribution of *P* mostly results from its low and spatially varying long-term trend (Extended Data Fig. 3e,f). Beside the comparison among single drivers, we found that *LAI* effects are concordant in sign with the overall trends in the energy partitioning terms (Supplementary Fig. 2) over more than 63% of the vegetated land (red labels of quadrants in Fig. 3d-f) and explain a considerable fraction of their variance (45–63%, blue labels in Fig. 3d-f). These findings emphasize the importance of *LAI* trends in affecting the long-term variations in surface energy partitioning, in particular by amplifying the release of energy via latent heat (Fig. 2a,d,g and Supplementary Fig. 2).

Leaf control and plant functional type

The spatial distribution of plant functional types (Fig. 4a) modulates the effects of *LAI* changes on energy partitioning. In the observation period forests show a strong increase in *LAI*, predominantly driven by climate change and CO_2 fertilization[9], and provide the largest contribution to the global signal of greening (48%, Fig. 4b). However, they are typically characterized by a low sensitivity of the energy terms to *LAI* possibly due to a more conservative and even use of water resources supported by a deeper rooting system[32] and by their abundance in demand limited regions. Therefore, when the two terms are combined (greening and sensitivity, Eq. (4), Methods), forests contribute for 21-27% of the global effect (δZ^{LAI}, where *Z* is any of the energy terms). In contrast, natural grasses show lower greening rates compared to forests but larger sensitivity driven by the rapid dynamics of *LAI* and shallow soil moisture, which are typical of these ecosystems. This combination results in a contribution of 32-38% to the global effect of greening on the surface energy partitioning. Croplands, despite their limited fractional cover (25%), play a more important role in affecting the surface energy partitioning by contributing to 41-43% of the global signal. This derives from the combination of relatively high values of both sensitivity and greening (Fig. 4c-e), the latter one possibly driven by agricultural intensification, which occurred in many regions of the World during the past decades[33].

Possible sensitivity bias in land surface models

The ability of LSMs to reproduce the interplay between *LAI* and surface energy partitioning has important implications on prediction of future land-climate interactions [22]. To assess this ability we replicated the analysis performed on observation-driven products on an ensemble of ten state-of-the-art LSMs (TRENDY v7[34]). Model simulations show that the CO_2 effect on stomatal conductance substantially reduces the sensitivity of *LE* to changes in *LAI* (-11%, Fig. 5b, S1 scenario) to the point of offsetting the modest but significant signal originated from changes in climate (8%, Extended Data Fig. 6c11, S3-S1 scenario). This ultimately leads to a net signal of no change in sensitivity in the scenario where all factors (CO_2, climate and land use change) are varied (Fig. 5a, S3 scenario). This pattern, in combination with the predicted reduction of supply-limited zones (Extended Data Fig. 4b), leads to an overall decline in the coupling between *LE* and water availability. These simulated patterns are in clear contrast with those retrieved from observation-driven products (Fig. 1 and Extended Data Fig. 4a). Such divergence suggests that LSMs may overestimate the sensitivity to CO_2 and underestimate the biophysical response of ecosystems to changes in water availability. This pattern emerge also from the systematic model underestimation of the fraction of transpired water to the total evapotranspiration[35]. Under a scenario of warming this bias of LSMs could ultimately lead to an underestimation of summer droughts sustained by anticipated spring phenology[36]. In addition, the large spread across LSMs (Fig. 5a,b and Extended Data Fig. 6) highlights the large structural uncertainty in the model representation of the phenomena. In fact, even if the ensemble is driven with a common climate forcing, model structure and parameterization show a large effect on the energy partitioning[37].

Overall, focusing on the sensitivity derived over the whole period and assuming the observation-based sensitivity of *LE* to *LAI* as reference, the tested LSMs show an overestimation of the sensitivity over tropical and boreal zones and an underestimation over arid-temperate zones (average data-model discrepancy of 0.89±0.44 and 2.9±0.53 Wm^{-2} per unit *LAI* change, respectively) (Fig. 5c,d). Such differences are associated to the underestimation and overestimation of ΔLAI in the two regions, respectively (Fig. 5e). Models show sensitivities and *LAI* trends with bias of opposite sign with respect to observational retrievals over about half of the globe and such compensatory effects hide the effective data-model discrepancies in the resulting global effect of greening on the partitioning of the surface energy fluxes (Extended Data Fig. 7). While disparities with respect to observation-based findings are conditioned by the accuracy of satellite retrievals – particularly critical in the tropics where *LAI* estimations tends to saturate – these results emphasize the current uncertainty generated by the approximate model representation of key vegetation-mediated biophysical processes.

Conclusions

Our analysis provides observational evidence that changes in vegetation density (*LAI*) during the past three and a half decades have played an important role in the surface energy partitioning, by favoring the release of energy via *LE* over *H*. This increased control of vegetation appears plausibly connected to the exacerbation of water-limited conditions and the progressive increase in evaporative surface associated with the global greening, and occurs despite the counteracting effect of CO_2 fertilization on stomatal conductance. As land feedbacks on climate are linked to vegetation status and activity, future land geoengineering could play an important role in modulating the strength of that forcing[8]. Furthermore, our results reinforce the importance of considering the co-variability of soil moisture and vegetation dynamics for the effective appraisal of the land-atmosphere coupling (usually focused exclusively on soil moisture variability and patterns)[7], particularly in view of the expected increase in *LAI* (ref. [38]) and drought conditions[39] over most of the globe. Finally, our data-model comparison emphasizes the need to better account for the impact of vegetation changes in energy partitioning to improve climate model projections. Fostering model representation of vegetation-atmosphere interactions with observation-driven estimates will ultimately enhance the reliability of future climate predictions.

Corresponding author

Correspondence to Giovanni Forzieri

Acknowledgements

The study was funded by the FP7 LUC4C project (grant nr. 603542).

Author Contributions

G.F. and A.C. conceived and designed the study; D.G.M. and B.M. provided GLEAM data; C.J. and Y.R. produced the new archive of long-term BESS data and harmonized *LAI* datasets; K.Z. provided PLSH data; A.W., A.A., D.S.G., V.K.A., S.L., D.L., E.K., J.E.M.S.N., H.T., P.F. and S.S run TRENDY v7 simulations; R.A. harmonized land surface model simulations; G.F. analyzed the data, G.F. and A.C. interpreted the results and wrote the manuscript with contributions from all coauthors.

Competing Financial Interests

The authors declare no competing financial interests.

References

1. Findell, K. L., Gentine, P., Lintner, B. R. & Kerr, C. Probability of afternoon precipitation in eastern United States and Mexico enhanced by high evaporation. Nat. Geosci. 4, 434 (2011).

2. Pielke, R. A. Influence of the spatial distribution of vegetation and soils on the prediction of cumulus Convective rainfall. Rev. Geophys. 39, 151–177
3. Pitman, A. J. The evolution of, and revolution in, land surface schemes designed for climate models. Int. J. Climatol. 23, 479–510 (2003).
4. Seneviratne, S. I. et al. Investigating soil moisture–climate interactions in a changing climate: A review. Earth-Sci. Rev. 99, 125–161 (2010).
5. Dirmeyer, P. A. The terrestrial segment of soil moisture–climate coupling. Geophys. Res. Lett. 38, L16702 (2011).
6. Puma, M. J., Koster, R. D. & Cook, B. I. Phenological versus meteorological controls on land-atmosphere water and carbon fluxes. J. Geophys. Res. Biogeosciences 118, 14–29 (2013).
7. Williams, I. N. & Torn, M. S. Vegetation controls on surface heat flux partitioning, and land-atmosphere coupling. Geophys. Res. Lett. 42, 2015GL066305 (2015).
8. Bagley, J. E. et al. The influence of land cover on surface energy partitioning and evaporative fraction regimes in the U.S. Southern Great Plains. J. Geophys. Res. Atmospheres 122, 2017JD026740 (2017).
9. Zhu, Z. et al. Greening of the Earth and its drivers. Nat. Clim. Change 6, 791–795 (2016).
10. Anderson, R. G. et al. Biophysical considerations in forestry for climate protection. Front. Ecol. Environ. 9, 174–182 (2011).
11. Bonan, G. B. Forests and Climate Change: Forcings, Feedbacks, and the Climate Benefits of Forests. Science 320, 1444–1449 (2008).
12. Forzieri, G., Alkama, R., Miralles, D. G. & Cescatti, A. Satellites reveal contrasting responses of regional climate to the widespread greening of Earth. Science 356, 1180–1184 (2017).
13. Pitman, A. J. et al. Importance of background climate in determining impact of land-cover change on regional climate. Nat. Clim. Change 1, 472–475 (2011).
14. Berry, J. A., Beerling, D. J. & Franks, P. J. Stomata: key players in the earth system, past and present. Curr. Opin. Plant Biol. 13, 232–239 (2010).
15. Keenan, T. F. et al. Increase in forest water-use efficiency as atmospheric carbon dioxide concentrations rise. Nature 499, 324–327 (2013).
16. Zeng, Z. et al. Climate mitigation from vegetation biophysical feedbacks during the past three decades. Nat. Clim. Change 7, 432–436 (2017).
17. Wilson, K. B. et al. Energy partitioning between latent and sensible heat flux during the warm season at FLUXNET sites. Water Resour. Res. 38, 1294 (2002).
18. Sellers, P. J. et al. BOREAS in 1997: Experiment overview, scientific results, and future directions. J. Geophys. Res. Atmospheres 102, 28731–28769 (1997).
19. Baldocchi, D. et al. FLUXNET: A New Tool to Study the Temporal and Spatial Variability of Ecosystem–Scale Carbon Dioxide, Water Vapor, and Energy Flux Densities. Bull. Am. Meteorol. Soc. 82, 2415–2434 (2001).
20. Piao, S. et al. Evaluation of terrestrial carbon cycle models for their response to climate variability and to CO2 trends. Glob. Change Biol. 19, 2117–2132 (2013).
21. Duveiller, G. et al. Biophysics and vegetation cover change: a process-based evaluation framework for confronting land surface models with satellite observations. Earth Syst. Sci. Data 10, 1265–1279 (2018).
22. Forzieri, G. et al. Evaluating the Interplay Between Biophysical Processes and Leaf Area Changes in Land Surface Models. J. Adv. Model. Earth Syst. 10, 1102–1126 (2018).

23. Jiang, C. et al. Inconsistencies of interannual variability and trends in long-term satellite leaf area index products. Glob. Change Biol. 23, 4133–4146 (2017).
24. Fan, Y., Li, H. & Miguez-Macho, G. Global Patterns of Groundwater Table Depth. Science 339, 940–943 (2013).
25. Morisette, J. T. et al. Tracking the rhythm of the seasons in the face of global change: phenological research in the 21st century. Front. Ecol. Environ. 7, 253–260 (2009).
26. Miralles, D. G., Gentine, P., Seneviratne, S. I. & Teuling, A. J. Land–atmospheric feedbacks during droughts and heatwaves: state of the science and current challenges. Ann. N. Y. Acad. Sci. 0, (2018).
27. Zhang, Y. et al. Multi-decadal trends in global terrestrial evapotranspiration and its components. Sci. Rep. 6, 19124 (2016).
28. Cheng, L. et al. Recent increases in terrestrial carbon uptake at little cost to the water cycle. Nat. Commun. 8, 110 (2017).
29. Zeng, Z., Peng, L. & Piao, S. Response of terrestrial evapotranspiration to Earth's greening. Curr. Opin. Environ. Sustain. 33, 9–25 (2018).
30. Piao, S. et al. Plant phenology and global climate change: Current progresses and challenges. Glob. Change Biol. 25, 1922–1940 (2019).
31. Forzieri, G., Alkama, R., Miralles, D. G. & Cescatti, A. Response to Comment on "Satellites reveal contrasting responses of regional climate to the widespread greening of Earth". Science 360, eaap9664 (2018).
32. Mokany, K., Raison, R. J. & Prokushkin, A. S. Critical analysis of root : shoot ratios in terrestrial biomes. Glob. Change Biol. 12, 84–96
33. Chen, C. et al. China and India lead in greening of the world through land-use management. Nat. Sustain. 2, 122–129 (2019).
34. Quéré, C. L. et al. Global Carbon Budget 2018. Earth Syst. Sci. Data 10, 2141–2194 (2018).
35. Lian, X. et al. Partitioning global land evapotranspiration using CMIP5 models constrained by observations. Nat. Clim. Change 8, 640 (2018).
36. Buermann, W. et al. Widespread seasonal compensation effects of spring warming on northern plant productivity. Nature 562, 110 (2018).
37. Jiménez, C. et al. Global intercomparison of 12 land surface heat flux estimates. J. Geophys. Res. Atmospheres 116, (2011).
38. Mahowald, N. et al. Projections of leaf area index in earth system models. Earth Syst Dynam 7, 211–229 (2016).
39. Dai, A. Increasing drought under global warming in observations and models. Nat. Clim. Change 3, 52–58 (2013).

Methods

Vegetation dynamics

Three satellite-based *LAI* products were used to analyze the changes in global vegetation for the period 1982–2016 derived from the Global Land Cover Facility (GLASS v3[40], http://ftp.glcf.umd.edu/), the Global Inventory Modeling and Mapping Studies Normalized Difference Vegetation Index (GIMMS3g v1[41], http://sites.bu.edu/cliveg/datacodes/) and the NOAA Climate Data Record (TCDR v4[42], ftp://eclipse.ncdc.noaa.gov/). The Monthly mean 1°

LAI was calculated by averaging *LAI* values from each product's original spatio-temporal resolution. The residual data gaps were filled by the Harmonic Analysis of Time Series (HANTS) method[23]. The growing season averaged *LAI* was used as a proxy of vegetation growth in this study. To this aim a climatological growing season spanning over months with at least 75% of days in greenness phase was derived from the Vegetation Index and Phenology satellite-based product[43] (VIP, https://vip.arizona.edu/vipdata/V4/DATAPOOL/PHENOLOGY/) and utilized as reference period to derive a multi-year time series of growing season *LAI*. Nonparametric Mann-Kendall trend tests were then computed at pixel level after averaging the *LAI* value over a 3°x3° spatial moving window separately for each product (Supplementary Fig. 3). The moving window aimed to preserve spatial consistency with the retrievals of sensitivity of energy partitioning terms to *LAI* (see next section). A sensitivity analysis of interannual variation and trend in *LAI* on the different thresholds used to identify the growing season was performed to corroborate the robustness of our results (Supplementary Fig. 4).

Results are explored for different climate zones, derived from the Köppen-Geiger World map of climate classification[44], and for vegetated types (*V*) including forests (broadleaf and needleleaf trees), natural grasses and croplands. We used datasets of plant functional types (PFTs) derived from the annual land cover maps of the European Space Agency's Climate Change Initiative (ESA-CCI, https://www.esa-landcover-cci.org/)[45] over the 2000–2014 period referring to a simplified aggregation scheme based on physiognomy alone. Based on such classifications scheme we derived the multi-annual average cover fraction of each vegetated class (F^V). Desert and semi-desert areas with average growing season *LAI* < 0.15 m^2m^{-2} were excluded from the analyses.

Energy partitioning terms and evapotranspiration products

We focused the analysis on the interplay between interannual variations in *LAI* and the terms of the surface energy partitioning, including latent heat (*LE*), sensible heat (*H*) and Bowen ratio (defined as $B=H/LE$) over the 1982–2016 period. *LE* was derived by combining latent heat of vaporization and evapotranspiration (*ET*) estimates derived from four different observation-based datasets including the Global Land Evaporation Amsterdam Model (GLEAM v.3.2a[46,47], https://www.gleam.eu/), the Model Tree Ensemble (MTE[48], https://www.bgc-jena.mpg.de/geodb/projects/Home.php), the Process-based Land Surface Evapotranspiration/Heat Fluxes (PLSH[49], http://files.ntsg.umt.edu/data/) and the Breathing Earth System Simulator (BESS[50], http://environment.snu.ac.kr/bess_flux/). The latter one represents a novel long-term *ET* product specifically developed for this study retrieved from a consolidated process-based model in combination with the three *LAI* satellite products utilized here. *H* was obtained from the closure of the energy balance by subtracting *LE* from the surface net radiation (*RN*), the latter term retrieved from the ERA-interim reanalysis data[51] (http://apps.ecmwf.int/datasets/). As such, the estimate of sensible heat implicitly includes the heat storage in canopy air and biomass and ground heat terms of the energy-balance equation. Transpiration and evapotranspiration data generated from GLEAM were also used to explore the trend in the fraction of transpired water to the total evapotranspiration *Tr*/*ET* (Extended Data Fig. 3i,j). Sensible fluxes derived from MTE[48] were used to verify the consistency of *H* estimates derived from the closure of the energy balance.

CO_2 concentrations may play a role in the interplay between changes in *LAI* and energy partitioning by leading to the partial closure of stomata and restricting the diffusion of water vapor out of leaves[15]. The use of PLSH and BESS, which explicitly integrate the CO_2 effect on stomatal conductance, allows accounting for such mechanisms. On the other hand, *LE* estimates based on GLEAM are independent from *LAI* (or other optical remote sensing metrics), which preserves the interplay between *LE* and *LAI* estimates from possible circularity effects. The vegetation status in GLEAM is characterized by the vegetation optical depth, a microwave-based vegetation parameter related to vegetation water content and biomass. In contrast, MTE, PLSH and BESS are based on a set of satellite-based predictors among which NDVI-derived fPAR estimates and *LAI* (Supplementary Table 2).

Inferring supply and demand limitation of *LE*

We inferred the primary limitation of *LE*, atmospheric demand or moisture supply, by comparing correlations between growing season averages of *LE* and growing season averages temperature and precipitation, in accordance with previous studies[4,52]. Growing season dates are derived from VIP surface phenological data[43] (as computed for *LAI*). Since temperature, radiation, and vapor pressure deficit are strongly correlated, temperature can be used as a proxy for atmospheric demand. We then compared the correlation between *LE* and precipitation ($\rho(LE, P)$) and correlation between *LE* and temperature ($\rho(LE, T)$), both computed over the whole time series spanning the 1982-2016 period, and defined supply-limited zones where $\rho(LE, P) > \rho(LE, T)$ and demand-limited zones where $\rho(LE, P) < \rho(LE, T)$. We then obtained a "static" classification map (moisture supply-limited vs. atmospheric demand-limited) resulting from the average of the multiple correlation maps obtained from the different *LE* (*ET*) products and climate data used in this study. Such clustering was used in combination with the vegetation map where only pixels with ≥ 80% of vegetated cover and ≤ 10% of irrigated area were included in the study domain (Supplementary Fig. 5). To this aim, we used the Global Map of Irrigation Areas (GMIA, http://www.fao.org/nr/water/aquastat/irrigationmap/index.stm) derived from statistical census data for the year 2005 (ref. [53]). Furthermore, in order to explore the temporal evolution of supply- and demand-limited zones we replicated the above-mentioned classification scheme over moving windows of different amplitude (7 and 13 years). This latter analysis produced a set of "dynamic" classification maps whose results are shown in Extended Data Fig. 4.

Sensitivity of surface energy partitioning on *LAI* changes

Sensitivity of surface energy partitioning terms (*LE*, *H* or *B* hereafter referred as *Z* for short) on *LAI* changes was initially computed at annual scale for the whole 1982–2016 period. It was expressed as the partial derivative resulting from a multiple linear regression relating the interannual differences in the *Z* component (ΔZ) to interannual differences in growing season averaged leaf area index (ΔLAI), annually averaged air temperature (ΔT), annually cumulated precipitation (ΔP), and annually averaged incoming shortwave radiation (ΔSW_{IN}):

$$\Delta Z = \beta_0 + \frac{\partial Z}{\partial LAI} \cdot \Delta LAI + \frac{\partial Z}{\partial T} \cdot \Delta T + \frac{\partial Z}{\partial P} \cdot \Delta P + \frac{\partial Z}{\partial SW_{IN}} \cdot \Delta SW_{IN}, \qquad (1)$$

T, SW_{IN} and P are the climate data used to derive each *ET* product (Supplementary Table 2) while *LAI* is retrieved from the satellite products described in the previous section (GLASS v3, GIMMS3g v3 and TCDR v4). All data have been linearly resampled prior to the analysis to the common 1°x1° spatial resolution. Eq. (1) is applied for each unique combination of energy fluxes and *LAI* dataset, therefore resulting in a 12-member ensemble of sensitivity estimates for each *Z* term. Such an approach based on the difference between two consecutive years (Δ operator) disentangles the resulting signal from possible long-term dependencies on covariates (e.g. the combined effect of rising temperatures and CO_2 concentrations on long-term *LAI* trends, as well as effects of long-term drying on soil moisture and biomass). The derived signal $\frac{\partial Z}{\partial LAI}$ integrates the bidirectional interactions between *LAI* and the Z term. To better sample the statistical inferences all predictors in Eq. 1 were quantified for each pixel over a centered 3°x3° spatial window. This approach factors out *LAI* impacts on energy fluxes that are triggered by a variation in the main climate drivers (e.g., increase in *P* triggering larger *LAI* and *LE* fluxes). However, the regression model in Eq. (1) assumes a linear interplay between response variable and predictors and does not account for the possible covariation amongst predictors. The use of such method, in place of more sophisticated techniques, appears a reasonable approach considering: 1) the length of the time series (35 years); 2) the choice of a parsimonious approach that can be applied consistently across different products and variables; 3) the ability to capture possible emergent first-order temporal changes in the signal.

Eq. 1 was also applied at monthly time scale separately for each *LAI* product. Monthly-scale sensitivity was computed by using growing season averaged *LAI* values and monthly-scale climate drivers in order to minimize the potential biases of satellite retrieval of *LAI* in snow cover conditions and to explore the effects of the changes in background climate. Note that monthly-scale Δ values for climate drivers are calculated as difference between the same months of two consecutive years. Furthermore, in order to better characterize soil moisture conditions, monthly-scale precipitation (*P*) accounts for concurrent and lagged cumulated precipitation whose contributions are derived from an empirically-derived decay exponential function under the assumption of 1m soil depth[54], as follows:

$$P_{t_0} = \sum_{i=0}^{n} \frac{P_i}{t_i - t_{i+1}} \left(1 - e^{-(t_i - t_{i+1})}\right) e^{-(t_i - t_0)}, \qquad (2)$$

where t_0 and t_i refer to the current month and the i-th lagged month, respectively.

Temporal variations in sensitivity of energy partitioning terms to *LAI*

In order to explore possible long-term variations in sensitivity of energy partitioning terms to *LAI* changes, Eq. (1) was also computed on annual scale over 7-year and 13-year temporal moving windows. This analysis was complemented with sensitivities estimated over two consecutive independent periods ranging from 1982 to 1999 (t1) and from 2000 to 2016 (t2). Absolute (Δ_{abs}) and relative (Δ_{rel}) changes in sensitivities were quantified and t-test was then used to determine if the two samples $\frac{\partial Z}{\partial LAI_{t2}}$ and $\frac{\partial Z}{\partial LAI_{t1}}$ were significantly different from each other. Temporal variations in sensitivity of sensible fluxes to *LAI* were also computed by using native estimates (H_n) directly provided by MTE. Results of this latter comparison are largely consistent with estimates obtained from *H=RN-LE* confirming the marginal effects of residual heat storage flux (Supplementary Fig. 6).

Potential effects of changes in satellite sensors

LAI datasets used in this study have been generated from time series of satellite observations that have been specifically harmonized to remove biases caused by changes in sensors. However, we cannot exclude that some residual effects of sensor change might still influence the year-to-year variations in *LAI* and thus the sensitivity of energy partitioning to *LAI* changes[23,55]. We therefore explored the variations in sensitivity recorded during the two afore-mentioned periods, 1982-1999 (t1) and 2000-2016 (t2) separately for each *LAI* product (Fig. S2). The split between these two periods reflects a major change in the monitoring system given the first year of Terra MODIS' operation in 2000, a sensor used in several *LAI* products in the t2 period. During the t1 period, *LAI* data were exclusively based on AVHRR acquisitions.

We evaluated the potential effects of changes in sensors by exploring the climate control on sensitivity ($\frac{\partial Z}{\partial LAI}$) for the t1 and t2 periods. To this aim, we expressed the sensitivity estimates as a function of the aridity index (AI)[56], quantified as:

$$AI = \frac{P}{T+33}, \qquad (3),$$

where *P* and *T* are the climatological estimates of annual cumulated precipitation and annual average temperature computed for the reference temporal period (Extended Data Fig. 2a,c,e). Based on the Kolmogorov-Smirnov significance test (p-value<0.05) we cannot reject the hypothesis that the two resulting samples come from the same distribution. In case of a systematic bias on the climatic control on $\frac{\partial Z}{\partial LAI}$ the two curves should have been statistically different.

Furthermore, we derived the sensitivity of energy fluxes to *LAI* changes for the whole 1982-2016 period using spatial gradient derived in a climatic space instead of temporal variability. For this purpose sensitivities have been binned in a precipitation-temperature (*PT*) space where every bin is therefore equally affected by variations in sensors, and where therefore gradients are independent form sensor changes over time (Fig. 1a,d,g). We then extrapolated annual sensitivity values ($\frac{\partial Z}{\partial LAI}^{PT}$) from the *PT* domain based on annual precipitation and temperature for each grid of the globe and for each year. Therefore, temporal changes in sensitivity derived with this second methodology are fully conditioned on the changes in climate (Extended Data Fig. 2b,d,f). The emerging temporal changes in $\frac{\partial Z}{\partial LAI}^{PT}$ show an increase in sensitivity of energy partitioning to *LAI* consistent with $\frac{\partial Z}{\partial LAI}$, therefore corroborating the role of environmental conditions as drivers of the increase in vegetation control on energy partitioning.

Effects of *LAI* trends on available surface energy partitioning

Variations in the surface energy partitioning associated with long-term variations in *LAI* (δZ^{LAI}) have been computed by applying the methodology described in ref. [12] and expressed by the following formulation:

$$\delta Z^{LAI} = \frac{\partial Z}{\partial LAI} \cdot \delta LAI, \qquad (4)$$

where δLAI is the long-term trend in growing season averaged *LAI* and $\frac{\partial Z}{\partial LAI}$ is the sensitivity of *Z* to *LAI* (Eq. 1) quantified over the 1982–2016 period (both at annual and monthly level). Consistently to the assessment of sensitivity, a 12-member ensemble of trend estimates was derived based on the different combinations of original *ET* and *LAI* products for each energy term. We implicitly assumed that the sensitivity $\frac{\partial Z}{\partial LAI}$, computed at interannual scale (Eq. (1)), is an appropriate metric to estimate the net climate impact on the phenomena. However, at longer time scale (from decades to century) additional ecosystem processes may emerge, such as adaptation phenomena driven by species change and shifting biomes, which could affect the future trends of the sensitivity. An indication on the long-term sensitivity in case of full adaptation can be derived from the analysis of the sensitivity in the spatial domain (Fig. 1a,d,g; Extended Data Fig. 2b,d,f)

In order to compare the *LAI* effects on the surface energy partitioning terms with those resulting from the other drivers of the regression, Eq. 4 was similarly applied to the sensitivities and long-term trend estimates of annually averaged *T*, *P* and SW_{IN}. The marginal effects of each single predictor have been quantified and compared with the overall trends in surface energy fluxes. The fraction of the overall trend in the energy term explained by a given predictor is then quantified as the ratio between the predictor-specific trend and the overall trend, both averaged globally.

Disentangling the human land-use management

We disentangled the marginal contribution of forests, natural grasses and croplands to the global signal of the long-term *LAI* effect on energy partitioning (δZ^{LAI}) computed at annual scale over the whole 1982-2016 period. The marginal contribution of a given vegetation type (Q^V) is derived utilizing the grid-cell cover fractions (F^V), as weights, based on the following equation:

$$Q^V(\delta Z^{LAI}) = 100 \cdot \frac{\sum_{i=1}^{n}(F_i^V \cdot A_i \cdot \delta Z^{LAI}{}_i)}{\sum_{i=1}^{n} A_i \cdot \delta Z^{LAI}{}_i}, \quad (5)$$

where *i* represents a pixel, *n* is the total number of vegetated pixels in the globe, δZ^{LAI} is the effect of a pixel, A_i is the area of a pixel that varies with latitudes. A similar approach was used to derive the marginal contribution of the different vegetation types on global land area, long-term trend in growing season averaged *LAI* (δLAI) and the sensitivity of the energy partitioning terms to *LAI* changes ($\frac{\partial Z}{\partial LAI}$). To characterize the biome-specific modulation effects on the *LAI*-energy interplay, we binned the cover fractions of each vegetation type as a function of δLAI and $\frac{\partial Z}{\partial LAI}$.

Furthermore, we derived a set of different land-use management conditions by excluding from the study domain all pixels with a fraction of croplands varying from 30% to 70%. We analyzed the relative changes in sensitivities over time (Δ_{rel})) and the climate control on the effects (δZ^{LAI}) for different land-use management conditions (cropland percentage). The latter one was determined by binning δZ^{LAI} as a function of the aridity index (Eq. (3)) and by testing the similarity of curves by the Kolmogorov-Smirnov test. Spatial and temporal patterns of sensitivity ($\partial Z/\partial LAI$) and effects (δZ^{LAI}) appears substantially independent on the crop coverage (Supplementary Fig. 7), therefore confirming the climate controls on the *LAI*-energy interplay even in vegetated lands subject to human land-use management.

Land surface model simulations

To complement the analysis based on observational products, we use simulations from ten state-of-the-art land surface models completed within the TRENDY v7 project[34] including: CABLE-POP, CLASS-CTEM, CLM5.0, DLEM, ISAM, JSBACH, JULES, LPX, ORCHIDEE-CNP, VISIT. All models provide prognostic estimates of *LAI* and *LE* (only two models provided *H*). In order to analyze the modeled relative contributions of external factors to changes in sensitivity of *LE* to *LAI*, we used factorial simulations obtained for the 1982–2016 period under different scenarios: changes in CO_2, climate and land use (S3, the most realistic scenario); changes in CO_2 only (S1) and changes in climate and land use only (S3-S1). For each run we quantify the modeled sensitivity of *LE* to *LAI* changes (Eq. 1) and the associated long-term effect (Eq. 4). Results for the climate and land use change scenario are obtained by subtracting the sensitivity computed under S1 to sensitivity computed under S3. Model results are compared with analogous estimates derived from satellite observation-based products and bias patterns explored across the gradient of the differences in absolute ΔLAI between data and models.

Multi-product ensembles

In order to better capture the emerging signals and account for the possible differences across *ET* and *LAI* products, we calculated the multi-product average trend in the surface energy partitioning *Z* term of the 12 experiments obtained for different observation-driven *LAI*–*ET* combinations. To derive a global estimate of the trend and related uncertainty and to fulfill the assumption of uncorrelated errors we subset the global domain extracting pixels with non-overlapping spatial windows, i.e. only pixel equally spaced 3 pixels in latitude and 3 pixels in longitude are selected. The sampling was replicated 9 times in order to progressively cover the full global domain. For each of the 9 global subsets (*D*) we derived the zonal median of trend, weighting each grid cell value based on its area. The global estimates of the trend in the *Z* term were quantified as the average of the estimates derived from the ensemble of the 9 global subsets. The analysis was replicated separately for each experiment. We then derived the average and the corresponding standard error of the ensemble of single-experiment global estimates. Similar procedures were employed to quantify the multi-product ensemble average and uncertainty of sensitivities and trend in growing season averaged *LAI*. Same approach is used for the ensemble of LSMs. We refer to average and standard error of the ensembles in text and figures where not differently indicated.

Data availability

The observation-driven datasets analyzed in this study are publicly available as referenced within the article. Simulations from ten Land Surface Models (CABLE-POP, CLASS-CTEM, CLM5.0, DLEM, ISAM, JSBACH, JULES, LPX-Bern, ORCHIDEE-CNP, VISIT) are available from the TRENDY dataset via a request to S. Sitch. All generated data are available from the corresponding author on request.

Code Availability

The custom MATLAB (R2017b) code written to read and analyze data and generate figures is fully available on request from the corresponding author.

References

40. Xiao, Z. et al. Long-Time-Series Global Land Surface Satellite Leaf Area Index Product Derived From MODIS and AVHRR Surface Reflectance. IEEE Trans. Geosci. Remote Sens. 54, 5301–5318 (2016).

41. Zhu, Z. et al. Global Data Sets of Vegetation Leaf Area Index (LAI)3g and Fraction of Photosynthetically Active Radiation (FPAR)3g Derived from Global Inventory Modeling and Mapping Studies (GIMMS) Normalized Difference Vegetation Index (NDVI3g) for the Period 1981 to 2011. Remote Sens. 5, 927–948 (2013).
42. Claverie, M., Matthews, J. L., Vermote, E. F. & Justice, C. O. A 30+ Year AVHRR LAI and FAPAR Climate Data Record: Algorithm Description and Validation. Remote Sens. 8, 263 (2016).
43. Zhang, X., Tan, B. & Yu, Y. Interannual variations and trends in global land surface phenology derived from enhanced vegetation index during 1982–2010. Int. J. Biometeorol. 58, 547–564 (2014).
44. Kottek, M., Grieser, J., Beck, C., Rudolf, B. & Rubel, F. World Map of the Köppen-Geiger climate classification updated. Meteorol. Z. 15, 259–263 (2006).
45. ESA. Land Cover CCI Product User Guide Version 2. (2017).
46. Miralles, D. G. et al. Global land-surface evaporation estimated from satellite-based observations. Hydrol. Earth Syst. Sci. 15, 453–469 (2011).
47. Martens, B. et al. GLEAM v3: satellite-based land evaporation and root-zone soil moisture. Geosci Model Dev 10, 1903–1925 (2017).
48. Jung, M. et al. Global patterns of land-atmosphere fluxes of carbon dioxide, latent heat, and sensible heat derived from eddy covariance, satellite, and meteorological observations. J. Geophys. Res. Biogeosciences 116, G00J07 (2011).
49. Zhang, K. et al. Vegetation Greening and Climate Change Promote Multidecadal Rises of Global Land Evapotranspiration. Sci. Rep. 5, 15956 (2015).
50. Jiang, C. & Ryu, Y. Multi-scale evaluation of global gross primary productivity and evapotranspiration products derived from Breathing Earth System Simulator (BESS). Remote Sens. Environ. 186, 528–547 (2016).
51. Dee, D. P. et al. The ERA-Interim reanalysis: configuration and performance of the data assimilation system. Q. J. R. Meteorol. Soc. 137, 553–597
52. Jung, M. et al. Recent decline in the global land evapotranspiration trend due to limited moisture supply. Nature 467, 951–954 (2010).
53. Siebert, S. et al. A global data set of the extent of irrigated land from 1900 to 2005. Hydrol. Earth Syst. Sci. 19, 1521–1545 (2015).
54. Pan, F., Peters-Lidard, C. D. & Sale, M. J. An analytical method for predicting surface soil moisture from rainfall observations. Water Resour. Res. 39, 1314 (2003).
55. Tian, F. et al. Evaluating temporal consistency of long-term global NDVI datasets for trend analysis. Remote Sens. Environ. 163, 326–340 (2015).
56. Köppen, W. Die Klimate der Erde: Grundriss der Klimakunde. (Berlin und Leipzig: Walter de Gruyter und Co, 1923).

Figure Captions

Figure 1. Sensitivity of surface energy partitioning to *LAI* changes. (**a**,**d**,**g**) Sensitivity of latent heat ($\frac{\partial LE}{\partial LAI}$), sensible heat ($\frac{\partial H}{\partial LAI}$) and Bowen ratio ($\frac{\partial B}{\partial LAI}$) to *LAI* changes computed for the 1982–2016 period and binned as a function of climatological mean precipitation (*P*, on the x-axis) and air temperature (*T*, on the y-axis). Black dots show bins with average values statistically different from zero (t-test; p-value≤0.05). (**b**,**e**,**h**) Temporal variations of sensitivities (ensemble average ± standard error) computed over a 13-year moving window for moisture supply- and atmospheric demand-limited regions and the whole globe. (**c**,**f**,**i**) Temporal variations of sensitivities computed separately over the 1982–1999 and 2000–2016 periods for different regions and expressed in terms of absolute variations (Δ_{abs}, on the x-axis) and relative variations (Δ_{rel}, on the y-axis). Results for each single *LAI*-*ET* combination are shown with different symbols; those with a black outline represent ensemble averages (both computed for each *ET* product and for the whole set of combinations labelled as "Ensemble" in legend), while overlaid black dots indicate statistically significant changes in sensitivity (t-test, p-value≤0.05). The spatial domains of supply- and demand-limited regions are shown in Supplementary Fig. 5.

Figure 2. Changes in surface energy partitioning associated with long-term trends in *LAI*. Spatial pattern (**a**), seasonal variability (**b**) and climate space (**c**) of *LAI*-related trend in latent heat (δLE^{LAI}) computed for the 1982–2016 period. (**d-f**) and **(g-i)** as (**a-c**), but for the *LAI*-related trend in sensible heat (δH^{LAI}) and Bowen ratio (δB^{LAI}), respectively. Black dots in (**a**,**d**,**g)** show pixels where both ensemble average *LAI* trend and sensitivity are significant (Mann-Kendall test and t-test, respectively; p-value<0.05). Values in (**b**,**e**,**h**) are binned as a function of time (on the x-axis) and latitudinal gradient (on the y-axis) and black dots show bins with average values statistically different from zero (t-test; p-value<0.05). Values in (**c,f,i**) are binned as a function of climatological mean precipitation (*P*, on the x-axis) and air temperature (*T*, on the y-axis) and black dots as in (**b**,**e**,**h**).

Figure 3. Comparison of *LAI* and climate effects on surface energy partitioning. (**a-c**) Effects (x) of the long-term trends in *LAI*, temperature (*T*), precipitation (*P*) and short-wave incoming radiation (SW_{IN}) on the latent heat (δLE^{x}), sensible heat (δH^{x}), and Bowen ratio (δB^{x}) for moisture supply- and atmospheric demand-limited regions and the whole globe. Box plots represent the 12-member ensemble of observation-driven products. The spatial domains of supply- and demand-limited regions are shown in Supplementary Fig. 5. (**d-f**) Density plot of pixel values of overall trends (on the x-axis) in latent heat (δLE), sensible heat (δH), and Bowen ratio (δB) versus the corresponding *LAI*-related effect δLE^{LAI}, δH^{LAI} and δB^{LAI}, respectively (on the y-axis). Red labels report the fraction of global domain falling in each quadrant delineated by red lines, while blue circles show the global-scale estimates with labels referring to the fraction of the overall trend in the energy term explained by the *LAI* effect alone.

Figure 4. Contribution of different plant functional types (PFTs) to the *LAI* control on energy partitioning. (**a**) Spatial map of cover fractions of PFTs (forests, natural grasses and croplands). (**b**) Relative contribution of each PFT to the global land area (Area), long-term variations of *LAI* (δLAI), sensitivity of energy partitioning terms to *LAI* changes ($\partial Z/\partial LAI$), long-term effects in surface energy terms due to long-term variations of *LAI* (δZ^{LAI}), with the Z term as *LE*, *H* and *B*. (**c-e**) Cover fractions of PFTs binned as a function of the long-term variations of *LAI* (δLAI, on the y-axis) and the sensitivity of latent heat ($\frac{\partial LE}{\partial LAI}$), sensible heat

($\frac{\partial H}{\partial LAI}$) and Bowen ratio ($\frac{\partial B}{\partial LAI}$) to *LAI* changes (on the x-axis). Average values are shown for each PFT in circles.

Figure 5. Comparison of observational and land surface model results. (**a**) Temporal variations of the sensitivity of *LE* to *LAI* changes ($\frac{\partial LE}{\partial LAI}$) retrieved from an ensemble of ten LSMs (TRENDY v7) under the S3 scenario (changes in CO_2, climate and land use) and computed over 13-year moving windows for supply- and demand-limited regions and the whole globe (ensemble average ± standard error). Labels at the bottom of the panel report the relative changes in sensitivities between the 1982–1999 period and the 2000–2016 period (Δ_{rel}), '*' indicates the t-test significance with p-value≤0.05. The spatial domains of supply- and demand-limited regions are shown in Supplementary Fig. 5. (**b**) as (**a**) but for the S1 scenario (changes in CO_2 only). (**c**) Spatial patterns of the differences in $\frac{\partial LE}{\partial LAI}$ between LSMs and satellite-driven products (TRENDY S3 - SAT) computed for the 1982–2016 period as the median of all data-model combinations. (**d**) Values in (**c**) are binned as a function of climatological mean precipitation (P, on the x-axis) and air temperature (T, on the y-axis). (**e**) Values in (**c**) are binned as a function of satellite (on the x-axis) and modelled (on the y-axis) absolute *LAI* interannual variations. Black dots in (**c**) and (**d,e**) show pixels and bins with average values statistically different from zero (t-test; p-value<0.05).

Increased control of vegetation on global terrestrial energy fluxes

Giovanni Forzieri, Diego G. Miralles, Philippe Ciais, Ramdane Alkama, Youngryel Ryu, Gregory Duveiller, Ke Zhang, Eddy Robertson, Markus Kautz, Brecht Martens, Chongya Jiang, Almut Arneth, Goran Georgievski, Wei Li, Guido Ceccherini, Peter Anthoni, Peter Lawrence, Andy Wiltshire, Julia Pongratz, Shilong Piao, Stephen Sitch, Daniel S. Goll, Vivek K. Arora, Sebastian Lienert, Danica Lombardozzi, Etsushi Kato, Julia E.M.S. Nabel, Hanqin Tian, Pierre Friedlingstein, Alessandro Cescatti

Supplementary online material

Figs. 1 to 7

Tables 1 and 2

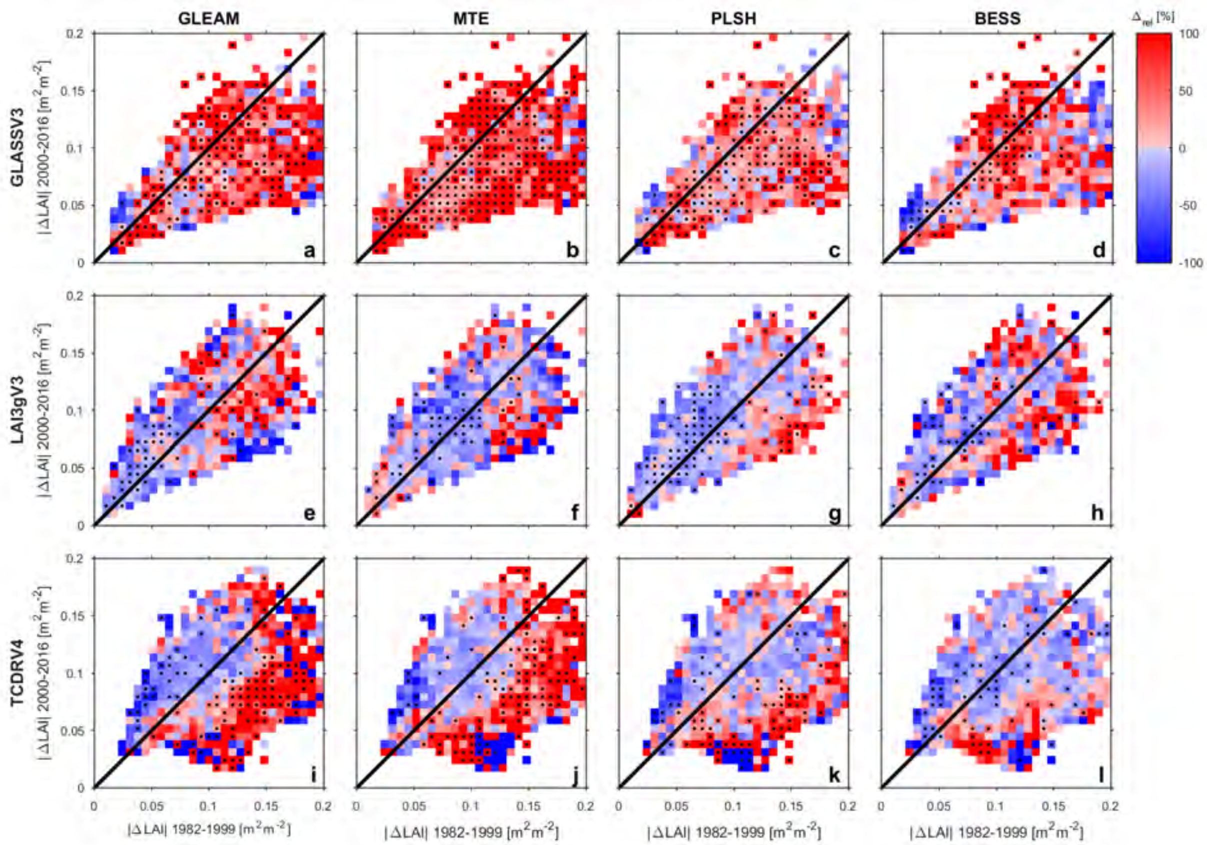

Figure 1. Relations between changes in sensitivity of *LE* to *LAI* and changes in inter-annual variations of *LAI* for single *LAI* and *ET* products. Relative variations of sensitivity of latent heat ($\frac{\partial LE}{\partial LAI}$) to *LAI* changes computed between the 1982-1999 period and the 2000-2016 period (Δ_{rel}, Methods). Values are binned as a function of absolute inter-annual variations in *LAI* recorded during the 1982-1999 period (on the x-axis) and absolute inter-annual variations in *LAI* recorded during the 2000-2016 (on the y-axis); black dots show bins where relative changes are statistically significant (t-test; p-value≤0.05).

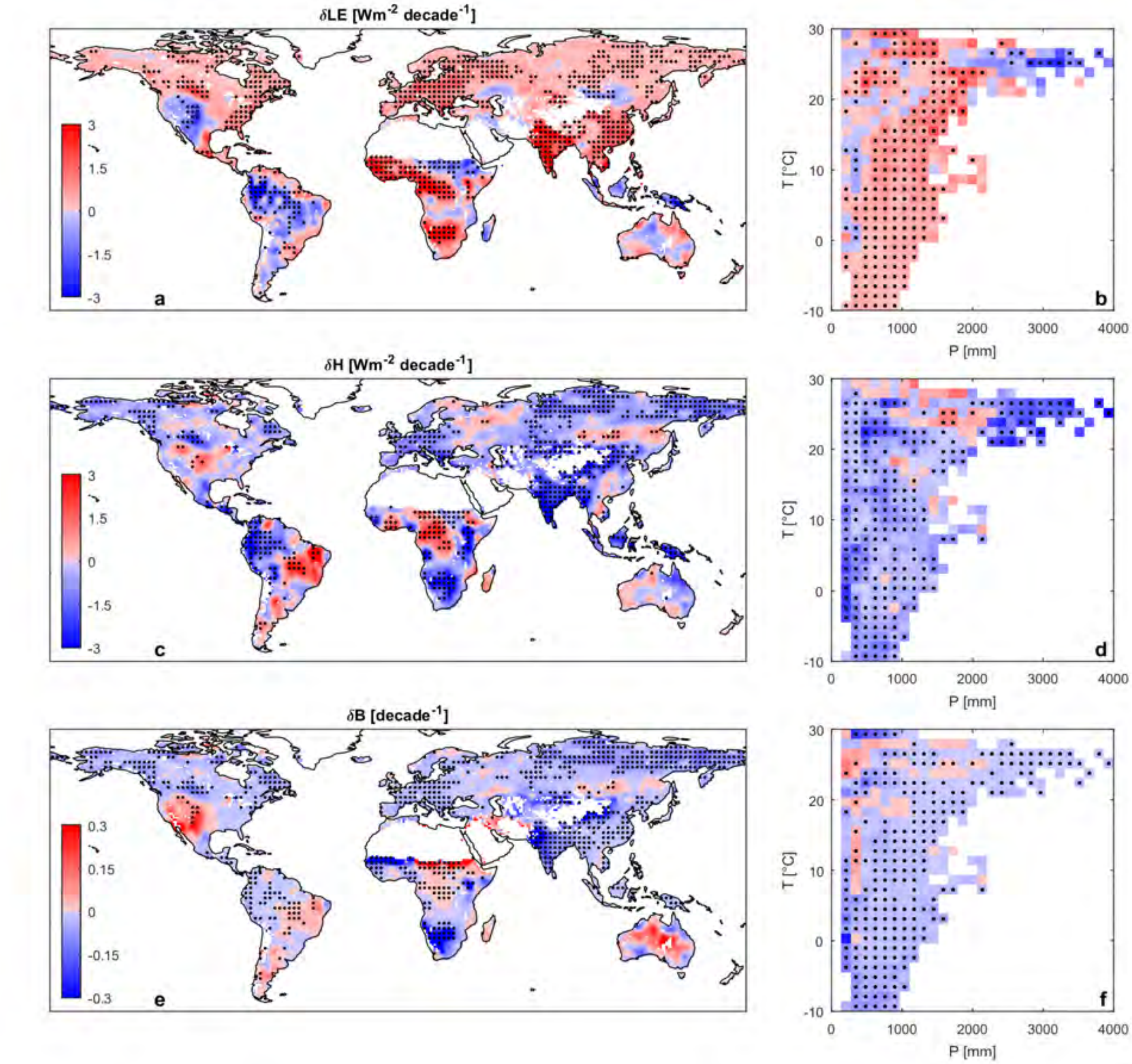

Figure 2. Overall trends in energy partitioning terms. Spatial patterns (**a**) and climate space (**b**) of long-term overall trend (1982–2016) in latent heat (δLE). (**c**,**d**) and **(e**,**f**) as (**a**,**b**) but for the sensible heat (δH) and Bowen ratio (δB). Areas in (**a**,**c**,**e**) labelled with black dots indicate trends that are statistically significant (Mann-Kendall test; p-value≤0.05). Values in (**b**,**d**,**f**) are binned as a function of climatological mean precipitation (P, on the x-axis) and air temperature (T, on the y-axis) and black dots show bins with average values statistically different from zero (t-test; p-value≤0.05).

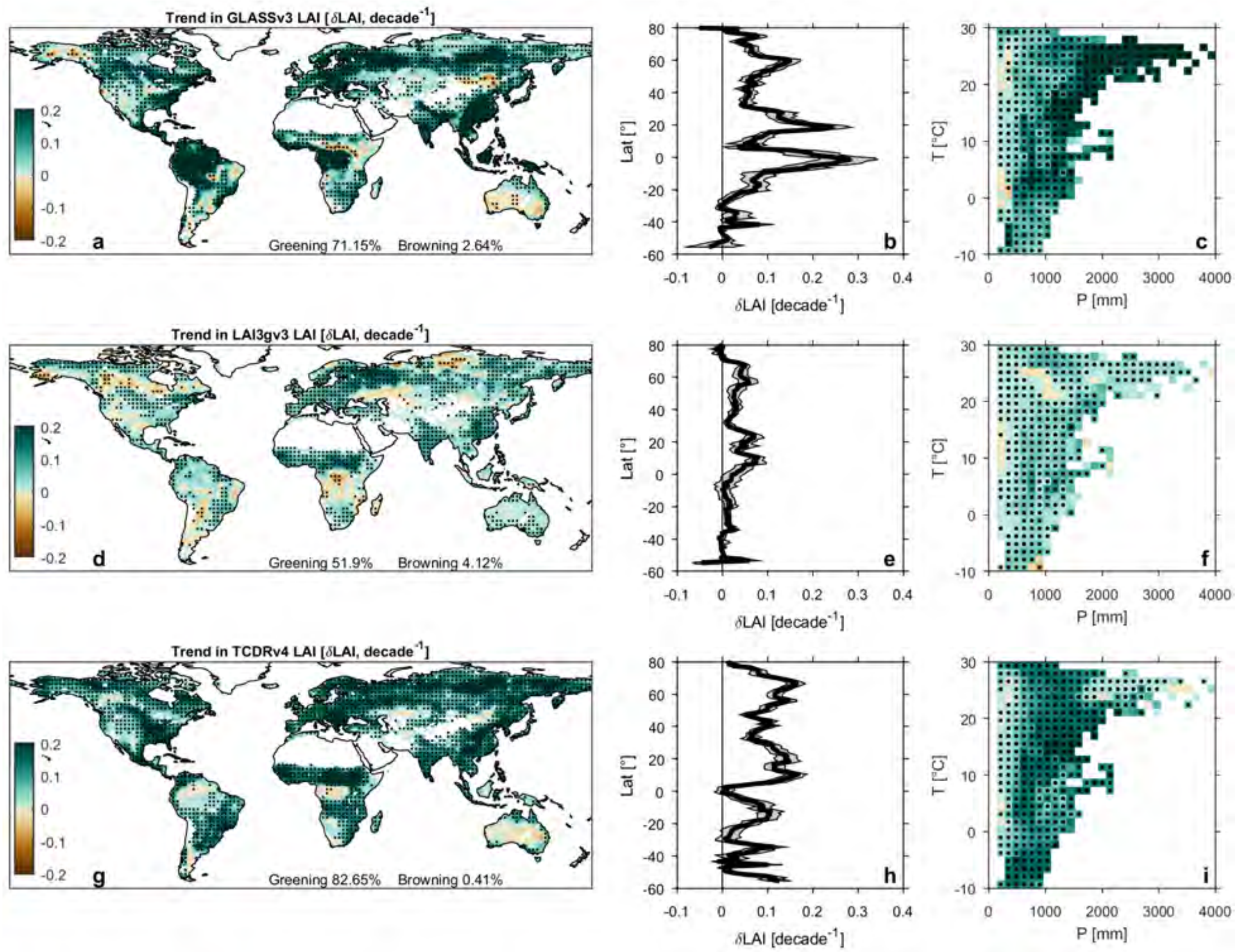

Figure 3. Trend in observed growing season averaged *LAI*. Spatial pattern (**a**), latitudinal profile (**b**) and climate space (**c**) of the trend in growing season averaged *LAI* (δLAI) derived from the GLASS v3 satellite product. Areas in (**a**) labelled with black dots indicate trends that are statistically significant (Mann-Kendall test; p-value≤0.05). Zonal median and confidence interval (standard error) of the latitudinal profile are shown in black line and grey shaded band in panel (**b**), respectively. Values in (**c**) are binned as a function of climatological mean precipitation (*P*, on the x-axis) and air temperature (*T*, on the y-axis) and black dots show bins with average values statistically different from zero (t-test; p-value≤0.05). (**d**-**f**) and (**g**-**i**) as (**a**-**c**) but for the GIMMS3g v3 and TCDR v4 satellite products, respectively. Labels "greening" and "browning" in (**a**,**d**,**g**) refer to the percentage area with a significant increase or decrease in *LAI*, respectively.

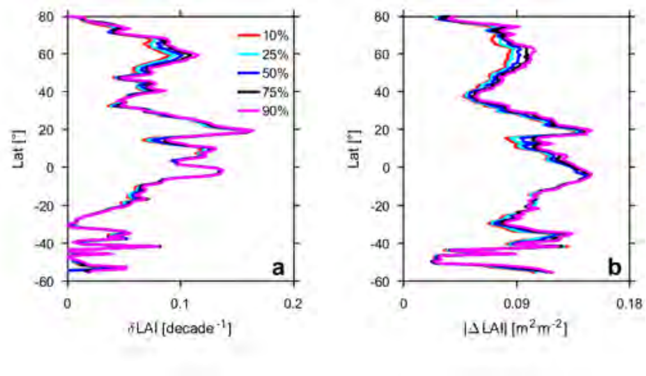

Figure 4. Sensitivity of trend and interannual variation of observed growing season averaged *LAI* to different definitions of greenness. (**a**) Latitudinal profile of the ensemble average trend in observed growing season *LAI* (δLAI). The growing season *LAI* is computed including months with a minimum percentage of days in greenness phase (Methods). Results for thresholds ranging between 10% and 90% are shown in different colors, as displayed in the legend. (**b**) as (**a**) but for the absolute interannual variation in *LAI* ($|\Delta LAI|$).

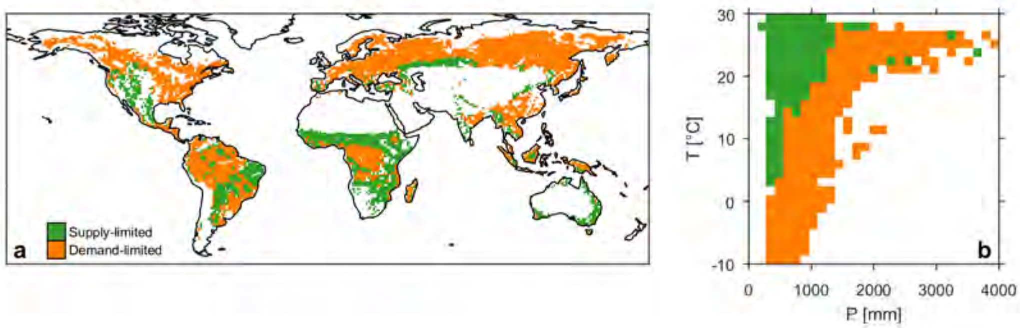

Figure 5. Spatial domain of supply- and demand-limited regions. (**a**) Spatial map of supply- and demand-limited regions. (**b**) Classes in (**a**) binned as a function of climatological mean precipitation (*P*, on the x-axis) and air temperature (*T*, on the y-axis).

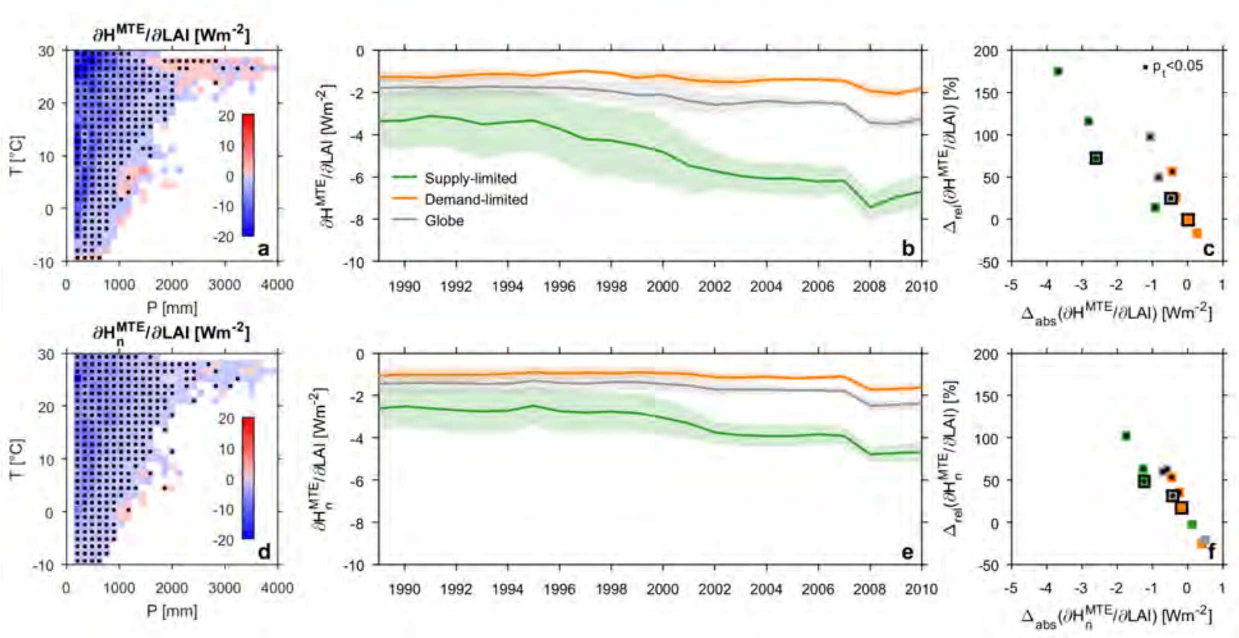

Figure 6. Comparison of spatial and temporal patterns of sensitivity of sensible fluxes to *LAI* changes for different retrieval approaches based on MTE data. (**a**) Sensitivity of sensible heat to *LAI* changes computed for the 1982–2016 period and binned as a function of climatological mean precipitation (*P*, on the x-axis) and air temperature (*T*, on the y-axis). Black dots show bins with average values statistically different from zero (t-test; p-value≤0.05). (**b**) Temporal variations of sensitivities computed over a 13-year moving window for moisture supply- and atmospheric demand-limited regions and the whole globe. (**c**) Temporal variations of sensitivities computed separately over the 1982–1999 and 2000–2016 periods for different regions and expressed in terms of absolute (Δ_{abs}, on the x-axis) and relative variations (Δ_{rel}, on the y-axis). Results for each single *LAI*-H^{MTE} combination are shown in separate markers; those with a black outline represent ensemble averages, while overlaid black dots indicate statistically significant changes in sensitivity (t-test, p-value≤0.05). Sensible fluxes are derived by subtracting *LE* from *RN*, with *LE* retrieved from MTE[46]. (**d**) as (**a**), (**e**) as (**b**) and (**f**) as (**c**) but derived from "native" *H* estimates directly provided by MTE. The spatial domains of supply- and demand-limited regions are shown in Supplementary Fig. 5.

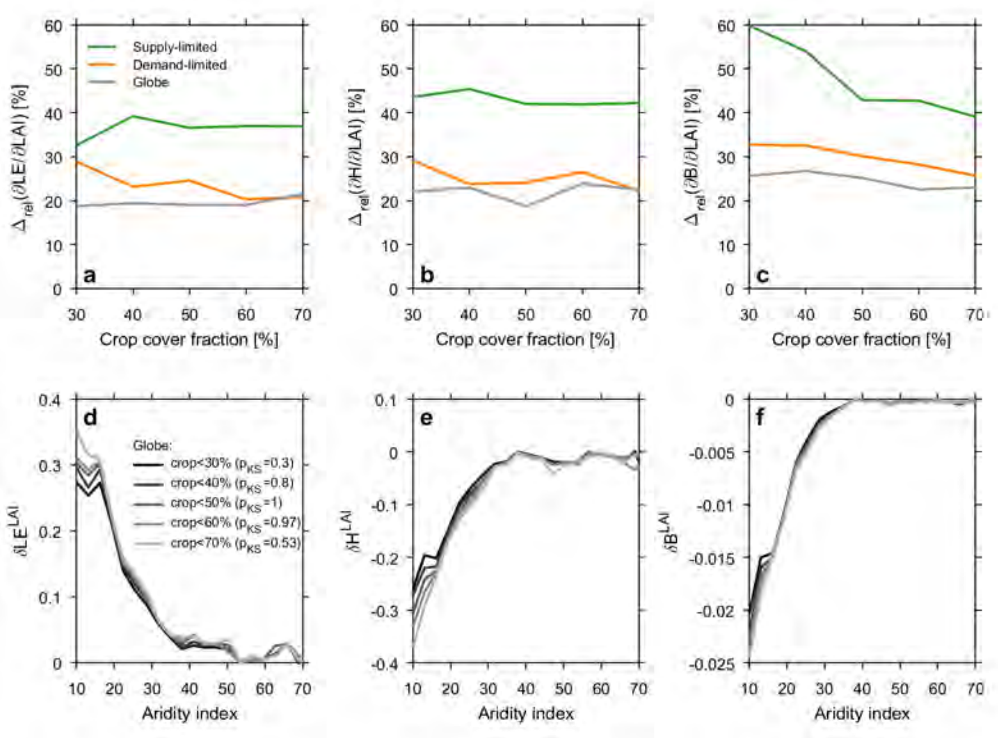

Figure 7. Spatial and temporal variations of sensitivity and effects as a function of human land-use management. (**a-c**) Relative variations of latent heat ($\frac{\partial LE}{\partial LAI}$), sensible heat ($\frac{\partial H}{\partial LAI}$) and Bowen ratio ($\frac{\partial B}{\partial LAI}$) to *LAI* changes computed separately over the 1982–1999 and 2000–2016 periods for different regions (Δ_{rel}, Methods) and across a gradient of crop fractions ranging between 30% and 70%. (**d-f**) Long-term effect of greening on latent heat (δLE^{LAI}), sensible heat (δH^{LAI}) and Bowen ratio (δB^{LAI}) computed for the whole 1982-2016 period (on the y-axis) binned as a function of the aridity index (on the x-axis) (Eq. (3), Methods). Results of the Kolmogorov-Smirnov test are shown in labels and reflects the significance level (p_{ks}) to reject the null hypothesis of dissimilar curve with respect to the 50% crop curve. The spatial domains of supply- and demand-limited regions are shown in Supplementary Fig. 5.

			δLAI [decade^{-1}]		$\frac{\partial LE}{\partial LAI}$ [Wm^{-2}]		$\frac{\partial H}{\partial LAI}$ [Wm^{-2}]		$\frac{\partial B}{\partial LAI}$ [-]		δLE^{LAI} [Wm^{-2}decade^{-1}]		δH^{LAI} [Wm^{-2}decade^{-1}]		δB^{LAI} [decade^{-1}]	
		#pixels	avg	s.e.	avg	s.e.	avg	s.e.	avg	s.e.	avg	s.e.	avg	s.e.	avg	s.e.
Supply-limited regions	All biomes	2011	0.066	0.023	8.183	0.869	-6.811	0.872	-0.333	0.034	0.413	0.088	-0.346	0.080	-0.017	0.003
Demand-limited regions	All biomes	4768	0.106	0.034	2.545	0.332	-2.140	0.288	-0.090	0.013	0.210	0.037	-0.166	0.034	-0.008	0.002
Globe	All biomes	6779	0.091	0.027	3.658	0.446	-3.256	0.409	-0.139	0.017	0.262	0.049	-0.220	0.047	-0.010	0.002

Table 1. Trends in growing season averaged *LAI*, sensitivity of surface energy partitioning terms to *LAI* changes and corresponding *LAI*-related trends for supply-, demand-limited zones and the whole globe. Values report the average value (avg) and the corresponding standard error (s.e.). The field “#pixels” expresses the sample size in terms of number of 1° grid cells.

ET	RN	T	P	SWin	Vegetation	CO2	Temporal coverage
GLEAM	ERAi	ERAi	MSWEP	ERAi	VOD	N	1982-2016
MTE	NA (ERAi)	CRU	GPCC	NA (ERAi)	fAPAR (GIMMS3g)	N	1982-2012
PLSH	NA (ERAi)	NCEP2	GPCP, GPCC, CRU	SRB, CERES	NDVI GIMMS3g	Y	1982-2015
BESS_LAI3gV3	NA (ERAi)	ERAi	NA (MSWEP)	ERAi	LAI GIMMS3g v3	Y	1982-2016
BESS_TCDRV4	NA (ERAi)	ERAi	NA (MSWEP)	ERAi	LAI TCDR v4	Y	1982-2016
BESS_GLASSV3	NA (ERAi)	ERAi	NA (MSWEP)	ERAi	LAI GLASS v1	Y	1982-2016

Table 2. Climate and vegetation drivers used in each ET product. Multiple linear regression models (eq. 1, Methods) use the climate dataset consistent for each ET product as reported in the table. In brackets are reported the reference dataset when no specific forcing (NA) is used for ET retrievals. Acronyms and sources of each climate product are described in the following lines:

- ERA-interim (ERAi, http://apps.ecmwf.int/datasets/);
- Climatic Research Unit ts 3.22 (CRU, http://www.cru.uea.ac.uk/cru/data/hrg/cru_ts_3.22);
- Multi-Source Weighted-Ensemble Precipitation v1.2 (MSWEP, http://www.gloh2o.org/);
- NCEP/DOE AMIP-II Reanalysis (NCEP2, https://www.cpc.ncep.noaa.gov/products/wesley/reanalysis2/);
- Global Precipitation Climatology Centre Version 6.0 (GPCC, https://www.esrl.noaa.gov/psd/data/gridded/data.gpcc.html);
- Global Precipitation Climatology Project Version 2.1 (GPCP, https://www.esrl.noaa.gov/psd/data/gridded/data.gpcp.html);
- World Climate Research Programme/Global Energy and Water-Cycle Experiment Surface Radiation Budget (SRB) Release-3.0 datasets https://gewex-srb.larc.nasa.gov/common/php/SRB_data_products.php);
- Clouds and the Earth’s Radiant Energy System (CERES, https://ceres-tool.larc.nasa.gov/ord-tool/jsp/SYN1degSelection.jsp)